Fabrication of Biocompatible Monolithic Microchannels with High Pressure-Resistance Using Direct Polymerization of PEG-Modified PMMA

Carmela De Marco,[1] Caterina Credi,[1] Francesco Briatico-Vangosa,[1] Elena Bianchi,[1] Ata Tuna Ciftlik,[2] Martin Gijs,[2] Gabriele Dubini,[1] Marinella Levi,[1] Stefano Turri[1]

[1]Dipartimento di Chimica, Materiali e Ingegneria Chimica "Giulio Natta", Politecnico di Milano, Piazza Leonardo da Vinci 32, 20133 Milan, Italy

[2]Laboratory of Microsystems, École Polytechnique Fédérale de Lausanne, CH-1015 Lausanne, Switzerland

Correspondence to: C. De Marco (E-mail: carmela.demarco@polimi.it)

Received 14 March 2014; accepted 13 May 2014

INTRODUCTION

Performing standard laboratory assays on a miniaturized Lab-on-Chip (LoC) device offers many benefits when compared to traditional techniques, including low analytes and samples consumption, reduced assay times, and improved sensitivity in measurements. Polymers are often used for fabricating LoC systems, since they offer optical transparency, biocompatibility, and are relatively easy to manufacture at a low cost.[1] Among such polymers, poly(methyl methacrylate) (PMMA) has been a popular choice, as PMMA is moderately hydrophilic,[2] which is in contrast with many other popular structural polymers that are inherently hydrophobic, like poly(dimethylsiloxane) (PDMS), therefore, necessitating additional surface modification steps to render the fabricated channels sufficiently hydrophilic or make them less prone to protein absorption for the desired operation.[3,4]

A number of microfluidic applications that involve high pressures also use microchannels fabricated with PMMA. For example, when applying high pressures required by inertial flow focusing for cytometry,[5] stiff materials, such as PMMA, could be used to ensure stability of the focusing over the microchannel cross-section geometry. Similarly, PMMA microchannels are used in fabrication of LoC systems for high-performance liquid chromatography,[6] and for the development of miniaturized systems to study droplet flows at high pressures.[7] Yet, previously reported PMMA–PMMA bonding methods cannot produce a bonding strength that is larger than 5.5 MPa,[8] hereby limiting the pressure-resistance of the microfluidic channels fabricated with such technology, mainly due to the detachment of PMMA layers when excessive pressure is applied.

In addition, the poor biocompatibility and protein biofouling properties of a surface of PMMA have also limited its usage for mass production in biological LoC systems.[9] While a number of methods have been proposed to modify the surface structure of the common structural polymers used for the microfabrication of LoCs to reduce their biofouling characteristics,[10,11] such surface treatments add laborious and time-consuming processes to the microfabrication process.[12] Consequently, a material that both is inherently biocompatible and can be used to fabricate high-pressure resistant microfluidic channels with a rapid, low

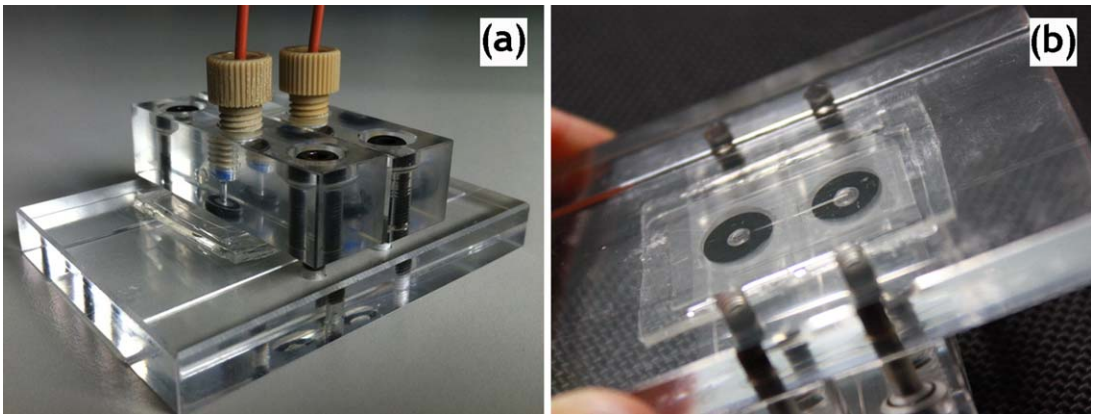

Figure 1. PMMA fluidic adapter used to perform burst pressure tests (a) and the sealing between the adapter and the microchip guaranteed by commercial O-rings (b). [Color figure can be viewed in the online issue, which is available at wileyonlinelibrary.com.]

cost, and simple process would be highly desirable for many applications of LoCs.

In this article, we present the use of a new material,[13,14] that is, a PEG-modified PMMA (PEGMA for brevity), for the fabrication of monolithic microchannels that can withstand pressures up to 12 MPa and that are inherently biocompatible.[13] This has been achieved by successive direct UV-photo partial polymerization of PEGMA layers through a printed photomask,[15] followed by a bonding step in which all layers are assembled by completion of the polymerization process, resulting in a rapid and low-cost method to produce microfluidic structures.

EXPERIMENTAL

Photopolymerization

The mixture to be polymerized had the following composition: 90.5% w/w tetraethylenglycol dimethacrylate, $M_w = 258$ g mol^{-1}, (Sigma Aldrich), 6% w/w PEG monomethacrylate, $M_w = 330$ g mol^{-1}, (PEGMA) (Sigma Aldrich), 3.5% w/w 2-hydroxy-2 methylpropiophenone (Darocur 1173, Ciba), the photoinitiator. The reagents were mixed in a dark glass vial in the desired ratio and stirred at room temperature for 5 min before use. Acetone was used to develop the devices and remove the residual monomer after photopolymerization. The equipment used for polymerization was a bromograph, model MF 1030 by Nuova Delta Elettronica, with four UV tubes ($\lambda = 365$ nm) 15 W each, equipped with a vacuum chamber. PDMS (Sylgard 184, Dow Corning) was used to obtain the frames and the cover used during the photopolymerization. The polyester photomasks were obtained printing at high definition (2500 dpi) on polyester photographic films (Alliance HS from AFGA) after creating the layout using AutoCAD software. Conversion of photopolymerization experiments was determined by DSC (Mettler Toledo) by evaluating the residual enthalpy of polymerization.[15]

Burst Pressure Tests

A custom PMMA fluidic adapter [Figure 1(a)], accepting commercial fluidic connectors and tubing (Upchurch Scientific), was used to connect microchips to a 2.5 mL stainless-steel high-pressure syringe (Harvard Apparatus) installed on an automated high-pressure syringe pump (Cetoni GmbH). The sealing between the microchip and the adapter was guaranteed by commercial O-rings (NBR 70 Shore A) [Figure 1(b)].

Following integration of the microfluidic chip within the PMMA adapter, the microchannels were filled with deionized (DI) water, and a valve placed to the exit lane was closed to block the fluid flow. During operation, the pressure at the device inlet was measured and recorded with a built-in commercial pressure sensor of the high-pressure syringe pump (Cetoni GmbH), which was installed at the inlet lane of the fluidic adapter.

Microscopy

We evaluated the shape and dimensions of microchannels and observed the fracture surface by scanning electron microscopy (SEM) (Zeiss EVO 50® Extended Pressure SEM system). Prior to observation, all the LoCs were cryofractured by immersing them into liquid nitrogen after the burst pressure test. Following this, a thin gold layer was sputtered by an Edwards High Vacuum International model S150B sputter and samples were subsequently transferred to the SEM system. After SEM imaging, the obtained images were analyzed using ImageJ software to measure the width and height of the channel, as well as the thickness of the cover lid.

Fouling-Release Dynamic Tests

Fouling-release capability of PEGMA was investigated using Bovine Serum Albumin Fluorescein Isothiocyanate (BSA-FITC) (Sigma–Aldrich) as the test protein. PMMA (Perspex™ by Lucite) were tested to benchmark the performances of PEGMA. Fouling-release dynamic tests were performed using a microfluidic pump (Syringe Pump 11 Plus, Harvard Apparatus) and a home-made microfluidic channel system. Micrometric channels were fabricated reversibly bonding a flat surface made of the chosen substrate material (PMMA or PEGMA) with a PDMS replica of an SU-8 channel (500 μm wide by 200 μm high). The albumin solution was then pumped into the microfluidic system at 7 μL min^{-1}and the test was stopped after 1 h. Finally, samples were rinsed by fluxing distilled water at 100 μL min^{-1} in the same channel. Observation by a fluorescence microscope (Olympus Ix70 inverted microscope) allows for the estimation of the protein adsorption on the substrates. Image elaboration was performed by ImageJ™ software which enabled us to

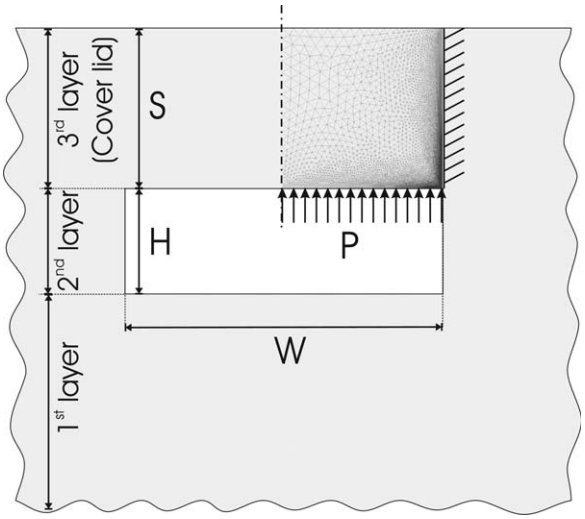

Figure 2. Schematic representation of the microchannel and of its finite element model. *S* is the channel lid thickness, and *W* and *H* are the channel width and height, respectively. The dashed-dotted line shows the axis used for symmetrical boundary condition, arrows indicate the direction of the applied pressure *P*, and mechanical ground on right-hand side indicates the fixed boundary.

obtain the graphical representation of the tonal distribution (image histogram) of digital fluorescent images for a quantitative comparison. The standard deviation was calculated averaging the mean tonal values of three different images for each sample material.

Finite Element Modeling of the Burst Pressure

To investigate the effects of the pressure and microchannel geometry on the LoCs behavior in burst tests, we performed a set of parametric analyses by finite element modeling (FEM), using COMSOL 4.1 simulation package. We modeled the behavior of the channel cover lid in two-dimensional as illustrated in Figure 2, under plane stress. Taking advantage of the symmetry, only one half of the cover lid was modeled. Further, to imitate a monolithic channel, the channel lid was described as rigidly bound to the edges. A distributed normal force, simulating the channel internal pressure, was applied to the inner surface of the channel while the outer surface was left load free. The material behavior was approximated as linear elastic with a Young's Modulus $E = 1.7$ GPa, a value that is determined from tensile tests, as described in the Supporting Information. We set a Poisson's ratio $v = 0.3$ that is typical for polymers. A very fine triangular mesh (with minimum mesh size 0.06 μm) was built close to the corner, since, at the fixed corners, the stress distribution is expected to possess a wedge-like singularity. Then, the mesh size was increased at increasing distance from the corner (see Figure 2).

RESULTS AND DISCUSSION

Fouling-Release Dynamic Tests

Image brightness is an indication of BSA-FITC adherence on the substrate. The fluorescent images show a greater signal intensity on PMMA [Figure 3(a)] with respect to PEGMA

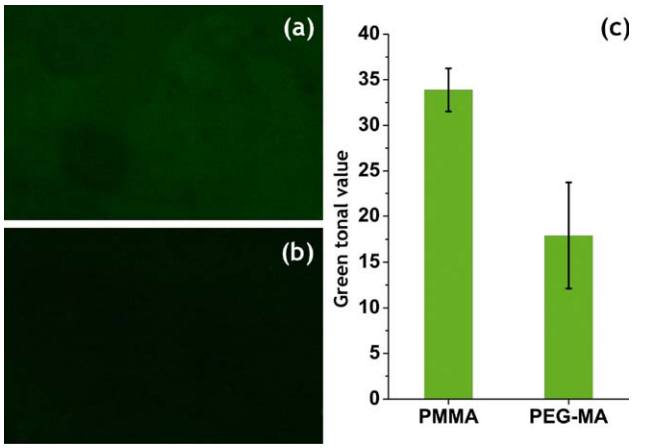

Figure 3. PMMA (a) and PEGMA (b) tested in dynamic conditions with BSA-FITC and observed by fluorescence microscopy (exposure time 200 ms, the substrate area observed is 400 × 270 μm^2). The mean tonal value for PMMA gives the brightest image while PEGMA blend the darkest. [Color figure can be viewed in the online issue, which is available at wileyonlinelibrary.com.]

[Figure 3(b)], indicating a better fouling-release behavior for the latter. A quantitative comparative analysis allows for the rationalization of the results, as shown in [Figure 3(c)].

Microchannels Fabrication

The fabrication process is composed of nine steps shown in Scheme 1(a–i). To obtain PEGMA microchannels, we used a simpler and more effective photopolymerization process than

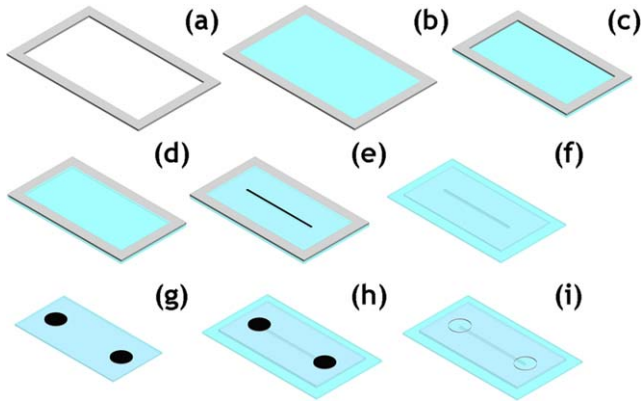

Scheme 1. Fabrication process of microfluidic channels using PEGMA photopolymerization. A 500 μm-thick PDMS frame is filled with the PEGMA mixture, covered with another PDMS layer (a), and UV-polymerized to obtain the first PEGMA layer (b). A second PDMS frame is placed over first PEGMA layer (c), filled with the PEGMA mixture (d), and covered with the polyester photomask containing the microchannel pattern (e). After UV-polymerization, we obtain the second layer with the grooved microchannel (f). Another PEGMA mixture was sandwiched between two masks, one mask having two circular reservoir patterns (g). By subsequent UV-polymerization, we obtain the third PEGMA layer that also acted as the channel lid. Finally, the third PEGMA layer was placed over the second one, and the entire system was UV-exposed (h), and completing the polymerization process, to obtain the monolithic microfluidic LoC (i). [Color figure can be viewed in the online issue, which is available at wileyonlinelibrary.com.]

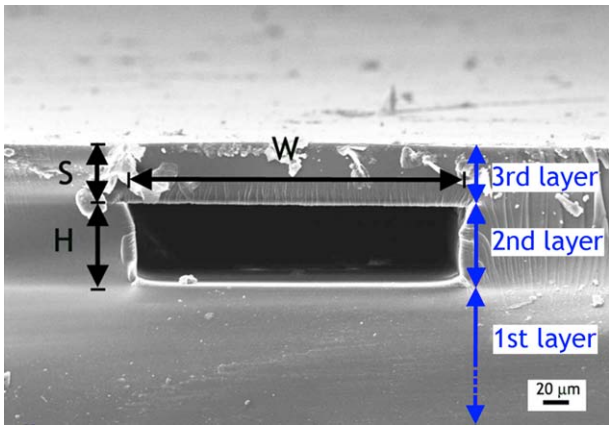

Figure 4. SEM image of a PEGMA microchannel cross section, where *H* and *W* are the height and the width of the microchannel, respectively, and *S* is the thickness of the channel lid (third layer). [Color figure can be viewed in the online issue, which is available at wileyonlinelibrary.com.]

that proposed in our previous work.[15] First, a thick PDMS layer (∼500 µm) was cut into a rectangular frame [Scheme 1(a)], filled with the PEGMA mixture, and covered with another PDMS layer to prevent the inhibition of polymerization by ambient oxygen. The PEGMA mixture was then photopolymerized during 52 s under UV light [corresponding to a kinetic conversion (KC) = 95%], to obtain the first PEGMA layer, shown in (b). Following this, a second rectangular PDMS frame was placed over the previously obtained first PEGMA layer (c), and filled again with the PEGMA mixture (d). Later, the polyester photomask pattern containing a 300 µm wide and 15 mm long microchannel layout was transferred to the underlying layer by a 30 s UV-polymerization (KC = 90%) (e), and rinsed with acetone to develop the nonexposed region. This gives the second PEGMA layer that contains the grooved microchannel as shown in (f). Separately, another PEGMA mixture was sandwiched between two photomasks, where the upper mask was patterned with two circular reservoirs that are 2 mm in diameter and 1.5 cm apart (g). With a 14 s UV-polymerization step (KC = 24 %), we obtained the third PEGMA layer containing inlet holes, which will act as the top lid of the microchannel. This third PEGMA layer containing the inlet holes was placed on the second one containing the microchannel groove, and the entire structure was exposed to UV during 180 s to seal all the layers together via completion of the polymerization process (h). The fabrication of PEGMA microfluidic channels was finalized by developing in acetone (i).

The SEM image in Figure 4 shows a cross section of a PEGMA microchannel fabricated with the presented technology. The height (*H*), which is determined by the second PEGMA layer thickness, the width (*W*) of the microchannel and the third PEGMA layer thickness (*S*) are indicated on the image. The three layers appear uniformly jointed without any apparent interface, leading to a monolithic microchannel. In the microfabrication process, we varied the microchannels dimensions in the range 225 µm $< W <$ 375 µm, while the microchannel lid thickness was in the range 83 µm $< S <$ 260 µm (See Supporting Information Figure S1 for more microchannels with different dimensions and aspect ratios).

Burst Pressure Measurements

We conducted burst pressure measurements with 12 fabricated microchannels with varying cross section dimensions and channel lid thickness. The pressure was adjusted in order to have approximately 0.1 MPa s^{-1} pressure increase rate and the pressure value at which an abrupt decrease was observed was taken as the burst pressure. Twelve microchannels were tested and with four of them we did not observe any rupture up to a pressure of ∼12 MPa, which is the pressure limit of the measurement set-up (due to fluid leakage from a strongly deformed O-ring).

The SEM observation of the microchannel cross section around the failure zones, as given in Figure 5, showed that no delamination between layers occurred, but rather the microchannel lid failed due to a cohesive fracture. This showed that the direct polymerization process presented here allowed the production of homogeneous channel structures without introducing any weakness at the bonding interface.

We also observed that the microchannel burst pressure was a function of the channel width *W* and the channel lid thickness *S*, in particular, their ratio *S/W*. To investigate this effect, we have plotted the burst pressure obtained by testing

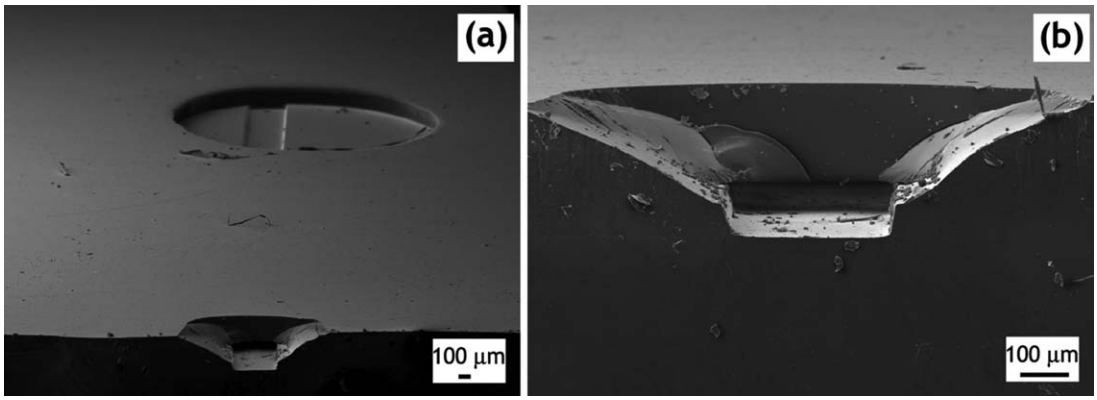

Figure 5. SEM image of a microchannel cross section around the failure zone. General overview of a broken structure, where the circular reservoir can be also observed (a), and magnified view of the corresponding failure zone (b).

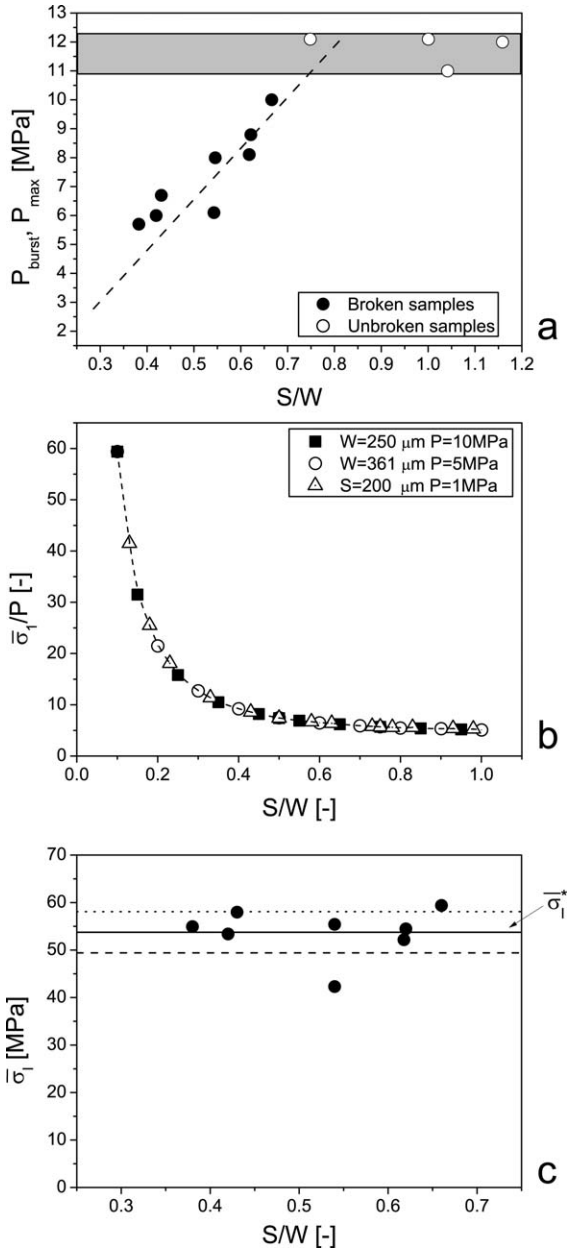

Figure 6. (a) Burst pressure versus channel-width-to-lid-thickness ratio *S/W*. Full points show burst pressure of failed samples, open points show the test results of those samples without failure, when the maximum allowed pressure of the test set up was reached. The dashed line is only intended as a visual aid. (b) Normalized stress $\bar{\sigma}_1/P$ as a function of channel lid thickness to channel width ratio *S/W*. Points show data from simulation at several *S/W* under different sets of channel dimensions *S*, *W*, and pressure *P*. The dashed line is just intended as a visual aid. (c) $\bar{\sigma}_1$ vs. channel-lid-thickness-to-channel-width ratio, *S/W*. The continuous line shows the mean value 54 ± 5 MPa, which is taken as the threshold stress $\bar{\sigma}_1^*$. Dotted and dashed lines show the lower and upper 95% confidence limit of the analysis.

microchannels with varying channel width *W* and lid thickness *S*, as shown in Figure 6(a). This plot indicates that the burst pressure in a channel increases with *S/W* ratio. In agreement with this observation, the samples with higher *S/W* ratios reach the maximum pressure allowed by the testing set-up without bursting, as reported in Figure 6(a) (open points).

Finite Element Modeling Simulation

To interpret the dependence of burst pressure on the *S/W* ratio, the effect of this variable was investigated by performing a series of simulations with the model described above, in which channel lid thickness, channel width, and applied pressure were varied separately. Due to the choice to model the material as linear elastic (see Supporting Information Figure S2), the stress is expected to show a singularity in the lower right corner of the model geometry (see Supporting Information Figure S3) and then to decrease leaving that point. Thus a radial system of coordinates was chosen with its origin in that corner, so that $\sigma_I = \sigma_I(r/W, \alpha)$ where r is the distance from the corner and α the angle with respect to the normal to the direction of application of the pressure. Once calculated the first principal stress field, we arbitrarily took as its significant value $\bar{\sigma}_I = \sigma_I(0.00285, 45^\circ)$. The angle $\alpha = 45^\circ$ was chosen as σ_I is observed to assume its maximum value at this angle, independent of both the *S/W* and *r/W* (see Supporting Information Figure S4), whereas $r/W = 0.00285$, corresponding to 1 μm for a channel width of 361 μm, was set in agreement to the mesh size. The choice of *r/W* as radial coordinate follows from the observation that $\sigma_I = \sigma_I(r/W, \bar{\alpha})$ curves from burst pressure test simulations coincide for any value of α in systems having different channel lid thickness (*S*) and channel width (*W*) but same *S/W* (see Supporting Information Figure S5).

Figure 6(b) shows the plot of the lid stress $\bar{\sigma}_I$normalized by the applied pressure *P* versus *S/W* ratio for three different scenarios related to the varying structural dimensions *S*, *W*, and the pressure *P*. In a first scenario, shown by filled squares, we chose a fixed pressure *P* of 10 MPa and channel width *W* of 250 μm, and the *S/W* ratio was swept between 0.1 and 1 by only varying the channel lid thickness *S*. After that, the first scenario was repeated with a fixed pressure *P* of 5 MPa and channel width *W* of 361 μm, where the data are shown by empty circles. Finally, the third scenario, shown by the empty triangles, fixes the channel lid thickness *S* to 200 μm and sweeps the *S/W* ratio by only varying the channel width *W* at a fixed pressure *P* of 1 MPa. The data clearly show that the variation of the normalized stress $\bar{\sigma}_1/P$ with the *S/W* ratio is actually independent of values of channel width *W*, channel lid thickness *S* and the applied fluidic pressure *P* alone.

Independently on model size and applied pressure the material undergoes a lower stress as the channel lid thickness increases at fixed channel width.

We show now that this normalized stress, which is independent of the individual dimensional parameters and pressures, can be used to estimate the strength of the material of the monolithic channel lid. For a monolithic channel lid, we can assume that there exists a threshold stress value $\bar{\sigma}_I^*$ above which the fracture occurs.

Looking at Figure 6(b), it is clear that in order to reach this threshold value, the pressure must increase as *S/W* increases, in agreement with the experimental findings of Figure 6(a). The

experimental data can in turn be used to cross-check the hypothesis and evaluate the $\bar{\sigma}_I$ value reached at burst by the LoCs tested in real experiments. The result in Figure 6(c) clearly shows that all sample burst at the same level of $\bar{\sigma}_I$, $\bar{\sigma}_I^* = 54 \pm 5$ MPa which can be therefore taken as representative of rupture.

Of course, $\bar{\sigma}_I^*$ must not be taken as an intrinsic critical property of the material, as its determination depends on a series of strong hypotheses and simplifications of the considered problem, and its validity is limited to the considered case. Nevertheless, it should be noticed that, apart from the numerical value of $\bar{\sigma}_I$, the same conclusions hold if the first principal stress is estimated somewhere else in the geometry, and that even if other quantities, such as, for example, von Mises stress, are taken in consideration, the same observations as in the case reported here hold. Thus, it may be affirmed that even if $\bar{\sigma}_I^*$is not an intrinsic critical property, it may be related with the strength of the PEG-based cover lid.

The fact that all samples show a similar threshold stress, $\bar{\sigma}_I^*$, represents a strong clue of the effectiveness of the LoCs preparation scheme presented in the article. The obtained results also imply that obtaining microchannels with controlled pressure-resistance is possible by simply choosing the appropriate lid thickness once the channel width is defined.

Finally, if the maximum vertical displacement (measured at the half width of the microchannel) due to the internal pressure is considered as a measure of the channel deformability, the simulations show that this quantity decreases from about 2.5 to 0.7 μm with increasing *S/W* ratio. Thus, besides controlling the pressure-resistance, it is possible to control the degree of channel deformability by selecting the proper lid thickness.

CONCLUSIONS

We presented the use of PEGMA as a structural material for the fabrication of monolithic polymer microchannels that can withstand pressures up to 12 MPa and are inherently biocompatible.[13] The fabrication process involved successive direct UV-photo polymerization of PEGMA liquid resin through printed photomasks. The SEM observation of the fractured microchannel cross sections after the burst pressure experiments showed no delamination between layers, but rather the failure of the microchannel lid due to a cohesive fracture. We later discovered that the burst pressure increases with the ratio *S/W*, where *S* and *W* are the channel lid thickness and width, respectively. FEM simulations allowed the assessment of the effect of geometry and load on the mechanical response of the cover layer. The outcomes of the model along with the experimental data allowed us to estimate a value for the first principal stress (determined in an arbitrary defined point of the geometry) similar for all the tested LoCs which can be taken as indicative of the material strength. The existence of an unique, rather high, value for this properties for all the tested devices is a strong clue of the effectiveness of the polymerization scheme performed in producing monolithic structures with a reproducible behavior.

We expect that the technique presented in this article will be a tool for rapid prototyping of monolithic channels and can open avenues for many applications requiring biocompatibility, high-pressure resistance, and limited channel deformation.

ACKNOWLEDGMENTS

The authors gratefully acknowledge financial support from the Fondazione CARIPLO (Contract no. 2010-0635) and the Italian Ministry of Education, University and Research (Programme Prin 2008). The authors thank Luca Masucci from GDP Prepress srl, Pero (Milan), for kindly providing the polyester photomasks. The authors also thank Dr. Francesco Caimmi for helpful discussions on the FEM model.

REFERENCES

1. Whitesides, G. M. *Nature* **2006**, *442*, 368.
2. De Marco, C.; Eaton, S. M.; Suriano, R.; Turri, S.; Levi, M.; Ramponi, R.; Cerullo, G.; Osellame, R. *ACS Appl. Mater. Interfaces* **2010**, *2*, 2377.
3. Ren, K.; Zhao, Y.; Su, J.; Ryan, D.; Wu, H. *Anal. Chem.* **2010**, *82*, 5965.
4. Zhou, J.; Khodakov, D. A.; Ellis, A. V.; Voelcker, N. H. *Electrophoresis* **2012**, *33*, 89.
5. Sollier, E.; Murray, C.; Maoddi, P.; Di Carlo, D. *Lab Chip* **2011**, *11*, 3752.
6. Kim, J. -Y.; Cho, S. -W.; Kang, D. -K.; Edel, J. B.; Chang, S. -I.; deMello, A. J.; O'Hare, D. *Chem. Commun.* **2012**, *48*, 9144.
7. Lorber, N.; Sarrazin, F.; Guillot, P.; Panizza, P.; Colin, A.; Pavageau, B.; Hany, C.; Maestro, P.; Marre, S.; Delclos, T.; Aymonier, C.; Subra, P.; Prat, L.; Gourdon, C.; Mignard, E. *Lab Chip* **2011**, *11*, 779.
8. Brown, L.; Koerner, T.; Horton, J. H.; Oleschuk, R. D. *Lab Chip* **2006**, *6*, 66.
9. Bi, H. Y.; Meng, S.; Li, Y.; Guo, K.; Chen, Y. P.; Kong, J. L.; Yang, P. Y.; Zhong, W.; Liu, B. H. *Lab Chip* **2006**, *6*, 769.
10. Chen, H.; Yuan, L.; Song, W.; Wu, Z. K.; Li, D. *Prog. Polym. Sci.* **2008**, *33*, 1059.
11. Banerjee, I.; Pangule, R. C.; Kane, R. S. *Adv. Mater.* **2011**, *23*, 690.
12. Liu, J. K.; Pan, T.; Woolley, A. T.; Lee, M. L. *Anal. Chem.* **2004**, *76*, 6948.
13. Turri, S.; Levi, M.; Emilitri, E.; Suriano, R.; Bongiovanni, R. *Macromol. Chem. Phys.* **2010**, *211*, 879.
14. De Marco, C.; Suriano, R.; Levi, M.; Turri, S.; Eaton, S.; Cerullo, G.; Osellame, R. *Microsyst. Technol.* **2012**, *18*, 183.
15. Suriano, R.; Levi, M.; Emilitri, E.; Momo, C.; Turri, S. *Macromol. Mater. Eng.* **2011**, *296*, 666.